



UNIVERSITY OF LEEDS

This is a repository copy of *Mixing performance and continuous production of nanomaterials in an advanced-flow reactor*.

White Rose Research Online URL for this paper:
<https://eprints.whiterose.ac.uk/170526/>

Version: Accepted Version

Article:

Yang, M, Yang, L, Zheng, J et al. (7 more authors) (2021) Mixing performance and continuous production of nanomaterials in an advanced-flow reactor. *Chemical Engineering Journal*, 412. 128565. p. 128565. ISSN 1385-8947

<https://doi.org/10.1016/j.cej.2021.128565>

© 2021, Elsevier. This manuscript version is made available under the CC-BY-NC-ND 4.0 license <http://creativecommons.org/licenses/by-nc-nd/4.0/>.

Reuse

This article is distributed under the terms of the Creative Commons Attribution-NonCommercial-NoDerivs (CC BY-NC-ND) licence. This licence only allows you to download this work and share it with others as long as you credit the authors, but you can't change the article in any way or use it commercially. More information and the full terms of the licence here: <https://creativecommons.org/licenses/>

Takedown

If you consider content in White Rose Research Online to be in breach of UK law, please notify us by emailing eprints@whiterose.ac.uk including the URL of the record and the reason for the withdrawal request.



eprints@whiterose.ac.uk
<https://eprints.whiterose.ac.uk/>

Mixing performance and continuous production of nanomaterials in an advanced-flow reactor

Mei Yang^{1#}, Lina Yang^{1#}, Jia Zheng^{2#}, Nicole Hondow¹, Richard A. Bourne¹, Tom Bailey¹,
George Irons¹, Elliot Sutherland¹, Daniela Lavric³, Ke-Jun Wu^{1,4*}

¹School of Chemical and Process Engineering, University of Leeds, United Kingdom

²School of Science, Dalian Maritime University, Dalian, China

³Corning S.A.S. Corning European Technology Centre, Avon, France

⁴College of Chemical and Biological Engineering, Zhejiang University, Hangzhou, China

Abstract

The Corning Advanced-Flow™ Reactor (AFR) whose productivity is ready for scale-up with limited loss of transport properties was implemented in the continuous synthesis of Ag nanoparticles (NPs). To demonstrate the effect of mixing on Ag NPs, the flow pattern and mixing characteristic (mainly on the meso- and macroscale) in AFR were studied by flow visualisation and computational fluid dynamics simulation first. It was found that increasing the total flow rate from 1 to 9 mL·min⁻¹ could enhance mixing by the synergetic combination of secondary flows created by different mechanisms. The flow rate ratio in the range of 0.25-8 affected the degree of mixing by changing the initial concentration distribution profile across the combined stream. The highest degree of mixing was obtained at the flow rate ratios of 0.25 and 8. Subsequently, the micromixing performance was quantified by Villermaux-Dushman method. The micromixing time decreased from 17 to 4 ms as the total flow rate increased from 1 to 9 mL·min⁻¹, while the micromixing time was nearly independent of the flow rate ratio. At last, the link between the mixing characteristics and average size and particle size distribution (PSD) of Ag NPs was established. As the total flow rate increased, the average particle size decreased, and PSD became narrower due to better micromixing efficiency. When the flow rate ratio varied, the PSD of Ag NPs was dependent on the width of the Ag precursor stream rather than the degree of mixing, because an excessive amount of NaBH₄ was used.

Keywords

continuous flow reactor, CFD simulation, mixing, continuous synthesis, nanomaterials

* Corresponding author, Tel.: +44-0113 34 30532, E-mail: k.j.wu@leeds.ac.uk

1 Introduction

1
2 Nanoscience and nanotechnology have become ubiquitous in our daily life [1]. Although
3
4 enormous scientific progress has been made in the synthesis and application of nanomaterials,
5
6 the cost-effective and scalable production of nanomaterials still holds the key to their
7
8 commercialisation [2]. A lot of promising nanomaterials technologies never reach the market
9
10 owing to issues with scale up to produce large quantities. If this aspect cannot be successfully
11
12 addressed, it may eventually struggle for widespread use. Nanomaterials are the trickiest to
13
14 scale up because the level of control that can be exerted on the nano- and microscales tends
15
16 to wane on the meso- and macroscale. The traditional protocols usually are developed based
17
18 upon batch processes, while such processes can always be finely tuned to obtain high quality
19
20 products in laboratory scale production, they usually fail to meet the requirements for large
21
22 scale production due to batch-batch variability, i.e. variability in the properties (chemical and
23
24 physical) of nominally identical nanomaterials obtained via repetitions of nominally the same
25
26 protocol [1, 3]. The variability may then lead to a considerable variation in the performance of
27
28 these materials, for instance, the characteristics of Ag and Au nanomaterials, such as particle
29
30 size and particle size distribution (PSD), are well known to have an effect on their catalytic
31
32 applications [4, 5], and for silica nanomaterials, particle properties such as morphology and
33
34 surface chemistry are known factors in determining biological impact [6]. Therefore, in order to
35
36 enter large scale production of nanomaterials with well-defined properties, high level of control
37
38 and robust, reproducible preparation methods are required. Continuous flow chemistry offers a
39
40 potential solution to overcome scale-up difficulties [7]. This type of chemistry is enabled by
41
42 using miniaturised continuous reactors (micro- and milli-reactors technologies), which possess
43
44 significant advantages over traditional batch technology [8-10]: (1) Micro- and milli-reactors,
45
46 with characteristic dimension varying from the micrometre to the millimetre scale, enable the
47
48 use of small amount of reagents, thereby dramatically decrease the costs of the process
49
50 screening and optimisation, and increase the safety of handling with hazardous reagents and
51
52 processes; (2) Attributed to their small characteristic dimension, they can provide a much
53
54 shorter diffusion distance, while larger surface area to volume ratio, and thus better mixing and
55
56 mass/heat transfer as compared to the traditional batch reactors from laboratory scale to
57
58 industrial scale; (3) Moreover, the throughput of these reactors can be increased by numbering-

1 up, e.g. arranging a reasonable number of micro-and milli-reactors in parallel, which facilitates
2 the transition from laboratory-developed processes to industrial applications.

3
4 Even though some successful cases have been reported using micro- and milli-reactors for
5 nanomaterials production, including Pd/graphene [11], Ag/Pd nanoparticles [12], Au
6 nanoparticles [13], perovskite nanocrystals [14], silica nanoparticles [15], and metal-organic
7 frameworks nanocrystals [16], numbering-up of these home-made micro-channel/micro-tubular
8 reactors with conventional non-standardised tubing, connectors, adaptors, etc. and non-
9 integrated heating/cooling elements for large scale production remains challenging [17]. One
10 of the commercial examples of continuous flow reactors, which has been used industrially, was
11 developed by Corning, known as Advanced-Flow™ Reactor (AFR). The Corning AFR is
12 comprised of a chain of identical cells with variable cross sections, internal obstacles, and an
13 integrated heat exchange system. The production capacity of the system can be easily
14 increased by switching to larger modules with a limited need for further optimisation [18] and
15 numbering-up with appropriate fluid distribution. These devices have been proven to work
16 successfully for homogeneous and heterogeneous organic synthesis processes [19-22],
17 however, there are few studies reporting applications for nanomaterials production, especially
18 for metal nanoparticles [23].

19
20 This study evaluated the performance of a Corning AFR (Lab Reactor Module) for
21 nanomaterials production, specifically the continuous synthesis of Ag NPs, in order to
22 understand the effects of mixing behaviour on nanoparticle synthesis and establish the process
23 at a larger scale. Generally, the mixing process is divided into three stages, i.e. micro-, meso-
24 and macromixing [24, 25]. Macromixing is defined as the mixing on the scale of the reactor;
25 that is how the fluid is distributed across the whole reactor. Mesomixing is on the scale of
26 vortices, generating engulfment and daughter vortices. Micromixing is on the scale of molecular
27 diffusion. The deformation of daughter vortices which are the outcome of mesomixing leads to
28 a lamellar structure where molecular diffusion occurs. To achieve our goal, flow visualisation
29 and computational fluid dynamics (CFD) simulations were conducted for methylene blue-water
30 system to characterise the flow pattern as well as mixing characteristic mainly on the meso-
31 and macroscale. Moreover, the mixing on the microscale was quantified by the Villermaux-
32 Dushman method (iodide-iodate reaction system). Inspired by the results obtained, an
33
34
35
36
37
38
39
40
41
42
43
44
45
46
47
48
49
50
51
52
53
54
55
56
57
58
59
60
61
62
63
64
65

1 optimised continuous synthetic protocol for Ag NPs in Corning AFR was proposed. Because
2 Corning AFR provides a wide range of throughput by increasing the channel size and number
3 of the unit simultaneously, while retaining mixing, mass/heat transfer performance, a seamless
4 transition from laboratory-optimized process to different-scale production could be achieved,
5 which have already been demonstrated in previous studies [26, 27].
6
7

8 **2 Experiments and methods**

9 **2.1 Materials**

10 Silver nitrate (AgNO_3 , Acros Organics), trisodium citrate dihydrate ($\text{Na}_3\text{CA}\cdot 2\text{H}_2\text{O}$, ≥ 99 wt.%,
11 Sigma Aldrich), sodium borohydride solution (NaBH_4 , 12 wt.% in 14 M NaOH, Sigma Aldrich),
12 methylene blue (MB, $\text{C}_{16}\text{H}_{18}\text{ClN}_3\text{S}\cdot 3\text{H}_2\text{O}$, 1% extinction, Fisher Bioreagents), potassium iodide
13 (KI, 99 wt.%, Alfa Aesar), potassium iodate (KIO_3 , 99.5 wt.%, Acros Organics), iodine (I_2 , >99
14 wt.%, Alfa Aesar), orthoboric acid (H_3BO_3 , >99.8 wt.%, BDH Laboratory Supplies), sodium
15 hydroxide (NaOH, $>97.5\%$, Scientific Laboratory Supplies), sulfuric acid (H_2SO_4 , 95-98 wt.%,
16 Honeywell Fluka), and bovine serum albumin (BSA, Sigma Aldrich) were purchased and used
17 as received without any further treatment. Deionised (DI) water (resistivity of $18.2 \text{ M}\Omega\cdot\text{cm}$) used
18 in all experiments was purified with Milli-Q ultra-pure water system.
19
20
21
22
23
24
25
26
27
28
29
30
31

32 **2.2 Corning AFR**

33 Figure 1 shows the structural details of the Corning AFR (Lab Reactor module) which is made
34 of glass. The AFR consists of three highly engineered fluidic layers, i.e., a reaction layer
35 sandwiched between two heat exchange layers (Figure 1a). The two heat exchange layers
36 have the same inlet and outlet, and the fluid in these two layers is guided by dashed-line walls.
37 The reaction layer, with an internal volume of 2.7 mL, is composed of a consecutive series of
38 heart-shaped cells with the same geometry (18 rows and 197 cells in total, Figure 1b). Each
39 cell contains a central U-shaped structure serving as an obstacle which forces the fluid to split
40 and recombine, along with the change of the flow direction. The cross-section of the channel
41 varies continuously along the flow direction, causing a position-dependent velocity profile. For
42 the reaction layer, AFR has two inlets (inlets 1 and 2 are marked in dark blue and yellow,
43 respectively, in Figure 1b) and one outlet (marked in green in Figure 1b). The fluid that enters
44 through inlet 1 is split into two streams before combining with the fluid from inlet 2 in the jet
45 zone (Figure 1c). The designed total flow rates for the reaction layer range from 2 to $10 \text{ mL}\cdot\text{min}^{-1}$
46
47
48
49
50
51
52
53
54
55
56
57
58
59
60
61
62
63
64
65

1, and the operation temperature and pressure ranges are -40 to 200 °C and up to 18 bar, respectively.

Figure 1 (a) Cross-sectional view of the Corning AFR Lab Reactor module showing the two heat exchange layers and the reaction layer, (b) Top view of the Corning AFR Lab Reactor module. The inlets 1 and 2 are marked in dark blue and yellow, respectively and the outlet is marked in green, (c) Enlarged image of top view of the Corning AFR Lab Reactor module. Streams 1 (S1) and 3 (S3) from inlet 1 combine with stream 2 (S2) from inlet 2 in the jet zone.

As shown in Figure 1c, the fluid from inlet 1 with a volumetric flow rate (Q_{inlet1}) is split into two streams (S1 and S3) with the same volumetric flow rate ($Q_{S1} = Q_{S3} = 0.5Q_{inlet1}$). These two streams combine with the fluid from inlet 2 ($Q_{inlet2} = Q_{S2}$) in the jet zone, then go through the nozzle into the first cell. The total volumetric flow rate (Q_{total}) and flow rate ratio (R) can be represented as follows:

$$Q_{total} = Q_{inlet1} + Q_{inlet2} = (Q_{S1} + Q_{S3}) + Q_{S2} \quad 1$$

$$R = Q_{inlet1}/Q_{inlet2} = 2Q_{S1}/Q_{S2} = 2Q_{S3}/Q_{S2} \quad 2$$

2.3 Flow visualisation

Because of the optical transparent feature of AFR, the flow pattern and mixing behaviour could be studied by a dye dilution-based characterisation method. A schematic diagram of the experimental setup is shown in Figure 2a. Aqueous methylene blue (MB) solution and colourless DI water were employed as the working fluids to be mixed. The two fluids were injected into the reaction layer from different inlets by syringe pumps (Chemyx, Fusion 100). The mixing phenomena of the two liquids were recorded by a CCD camera (15 frames per second, FLIR Grasshopper3 USB3, Model: GS3-U3-12S5C-C) mounted on a stereo microscope (Olympus, SZX16) at room temperature (20-22 °C). AFR was illuminated by a LED light source (Olympus, SZX2-ILLT) integrated with the microscope. The resolution of the recorded images was 2448×2048 pixels (i.e., 0.0087 mm/pixel).

Figure 2 (a) Experimental setup for flow visualisation using aqueous MB solution and DI water as the working fluids, (b) Relationship between the grey level and the concentration of MB.

To quantify the degree of mixing, the calibration between the grey level (ΔG) and the concentration of MB solution (C_{MB}) was carried out. MB solutions with known concentrations of 0.025, 0.05, 0.10, 0.15, 0.225, 0.30, 0.40, 0.50, and 0.60 mg/mL were prepared by dissolving a certain amount of MB into DI water. The prepared solutions were pumped into the reaction layer from the two inlets simultaneously. A set of calibration images was captured for each solution after the whole system appeared stable. The image processing was undertaken using Fiji (a distribution of ImageJ software):

(1) The captured RGB images were first converted into 8-bit grayscale images since it was more effective to analyse the combination of red, green and blue channels rather than each separate colour channel [28];

(2) To eliminate the effect of background, the background image, measured from the pure DI water, was subtracted from the original images;

(3) The correlation between the averaged grey level with the concentration of MB (determined with over 80 images, and the standard deviation was below ± 0.1) was then established and shown in Figure 2b.

Based on the ΔG - C_{MB} correlation, the concentration distribution profile in the region of interest (ROI) for each mixing experiment could be determined. The degree of mixing is widely quantified by the so-called mixing index (MI), which is an indicator of the quality of the mixing process [29, 30]. Several equations are widely used by the researchers to calculate MI [31]:

$$MI = 1 - \frac{\sigma}{\bar{C}} \quad 3$$

$$MI = 1 - \frac{\sigma}{\sigma_{\max}} \quad 4$$

$$\sigma = \sqrt{\frac{1}{N} \times \sum_{i=1}^N (C_i - \bar{C})^2} \quad 5$$

Where σ represents the standard deviation of the species concentration in the cross-sectional plane analysed, and N is the total number of pixels in the cross-sectional plane analysed. C_i and \bar{C} are the species concentration at the i^{th} pixel and the species concentration for complete mixing, respectively. σ_{\max} is the maximum standard deviation of the species concentration, and obtained by assuming no mixing occurs.

In Equation 3, a dimensionless mixing index is defined by comparing σ with \bar{C} . Most studies about mixers are carried out under the conditions that the two fluids to be mixed have the same

flow rate, i.e. the flow rate ratio is equal to 1. In this case, the mixing index calculated from Equation 3 is in the range of 0-1. 0 is for total segregation, while 1 is for complete mixing. However, when the flow rate ratio is not 1, the mixing index for total segregation is not equal to 0, and varies with the flow rate ratio (Table S1). Hence, it is difficult to compare the degree of mixing at different flow rate ratios by the mixing index determined by Equation 3. When studying the effect of the flow rate ratio, Equation 4 is always employed, in which σ_{\max} is introduced to normalise σ , and the value of σ_{\max} is dependent on the flow rate ratio [32, 33]. When the flow rate ratio is 1, the mixing index calculated from Equation 4 is equal to the value calculated from Equation 3. For all flow rate ratios, the mixing index calculated from Equation 4 lies between 0 and 1. The higher the mixing index, the greater the degree of mixing. In this section, the effects of the total flow rate and flow rate ratio on the flow and mixing characteristics were studied. The mixing indices at different operation parameters were calculated according to Equation 4. The corresponding experimental conditions were listed in Table S2. Because the flow rate ratio varied in a wide range from 0.25 to 8, the concentration of MB solution at the inlet was varied accordingly to maintain the outlet concentration of MB a constant, i.e., 0.2 mg/mL and thus achieve a high-contrast visualisation of the mixing process.

2.4 Computational fluid dynamics (CFD) simulation

Three-dimensional (3D) numerical simulation of the flow and mixing characteristics in the AFR was carried out using finite volume method on ANSYS Fluent 17.0 software. Based on the preliminary experimental work, the mixing was quite close to the ideal state within the first several cells in most cases. Therefore, the CFD simulation was performed only in the region from the inlet to the third cell to reduce the computational load of simulations. Considering the symmetry of the reactor structure, a 3D computational domain with only the top half of the channel as well as a symmetric boundary condition were adopted. Therefore, the equations governing the momentum and mass transports can be written as:

$$\text{Continuity equation} \quad \nabla \cdot \vec{v} = 0 \quad 6$$

$$\text{Navier-Stokes equation} \quad \rho \frac{\partial \vec{v}}{\partial t} + \rho \vec{v} \cdot \nabla \vec{v} = -\nabla P + \rho \vec{g} + \mu \nabla^2 \vec{v} \quad 7$$

$$\text{Species convective-diffusion equation} \quad \frac{\partial C}{\partial t} + \vec{v} \cdot \nabla C = D \nabla^2 C \quad 8$$

Where \vec{v} is the velocity vector, ρ is the density, μ is the dynamic viscosity, P is the pressure, C is the concentration of the species, and D is the diffusion coefficient of the species. Steady-

1 state, Newtonian and incompressible conditions were assumed to solve these equations, so
2 the transient term could be neglected. Moreover, the gravitational force could also be ignored
3 on the microscale [34].
4

5
6 Consistent with the flow visualisation, MB solution and DI water were employed as the working
7 fluids. During the simulation, the effects of the total flow rate and flow rate ratio on the flow
8 patterns and mixing characteristics were studied. Under different experimental conditions, the
9 mass fractions of MB at the inlet were kept the same as those used in the flow visualisation
10 (see Table S2 for details). The properties of the working fluids at room temperature (20 °C)
11 were adopted. Since the mass fraction of MB was at a very low level, the density and dynamic
12 viscosity of the MB solutions were set as $997 \text{ kg}\cdot\text{m}^{-3}$ and $1.0 \times 10^{-3} \text{ kg}\cdot\text{m}^{-1}\cdot\text{s}^{-1}$, respectively,
13 which are the same as those of water. The diffusion coefficient of MB in water was set as 0.674
14 $\times 10^{-9} \text{ m}^2\cdot\text{s}^{-1}$ [35]. The boundary conditions set up in the simulation to solve Equations 6-8 were
15 described as follows: (1) mass-flow-inlet for inlets 1 and 2, (2) outflow for the outlet, and (3) no-
16 slip condition at the channel wall. Generally, no-slip condition is valid when the Knudsen
17 number is ≤ 0.001 [36] and the Knudsen number in AFR was calculated to be smaller than the
18 order of 10^{-7} . Considering the total flow rate studied in this study ranging from 1 to 9 $\text{mL}\cdot\text{min}^{-1}$,
19 the simulation was performed using a laminar flow model. Hexahedral computational cells were
20 used to discretise the computational domain. A series of 3D grid systems with the cell number
21 ranging from 285971 to 919824 were carefully built. After the grid independence test (Figure
22 S1), a mesh consisting of 678176 hexahedral cells was adopted (Figure 3). Pressure-velocity
23 coupling was solved by SIMPLE (Semi Implicit Pressure Linked Equation) scheme. The
24 second-order upwind scheme for the momentum was employed for the spatial discretisation.
25 The iterative procedure was repeated until the residual met the criterion of 10^{-6} for all equations.
26
27
28
29
30
31
32
33
34
35
36
37
38
39
40
41
42
43
44
45
46
47
48

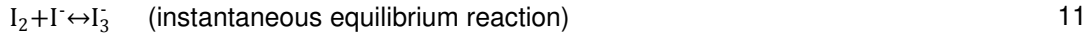
49 Figure 3 Schematic diagram of the mesh structure used in the 3D CFD simulation.
50
51

52 **2.5 Villermaux-Dushman method**

53

54 Due to the limited spatial resolution of the optical microscope, flow visualisation and CFD
55 simulation could mainly provide mixing information on the meso- and macroscale [37]. To get
56
57
58
59
60
61
62
63
64
65

more details about the mixing performance on the microscale, the Villermaux-Dushman method was employed, including the following parallel competing reactions:



The neutralisation of H_2BO_3^- ions (9) is quasi-instantaneous, while the Dushman reaction (10) is much slower than the neutralisation reaction, but in the same characteristic time scale with the micromixing process. As for perfect mixing, the H^+ ions are instantaneously consumed by H_2BO_3^- ions. The Dushman reaction cannot happen due to the stoichiometric defect of H^+ ions. In the case of imperfect mixing, a local stoichiometric excess of H^+ ions whose amount is larger than that required by neutralisation of H_2BO_3^- ions exists. Therefore, the H^+ ions are consumed competitively by the neutralisation of H_2BO_3^- ions and the Dushman reaction. The formed I_2 further reacts with I^- ions to yield I_3^- ions according to Equation 11. The amount of produced I_3^- ions depends on the micromixing efficiency and can be monitored by a UV-Vis spectrophotometer at 353 nm. The extinction coefficient of I_3^- was $25505 \text{ L}\cdot\text{mol}^{-1}\cdot\text{cm}^{-1}$ measured in this study, close to the value reported in the literature [38].

The experimental setup for the Villermaux-Dushman method was similar to that depicted in Figure 2a. The difference was that no image acquisition system was required in this section. All the experiments were carried out at room temperature (20-22 °C). In a typical experimental procedure, a solution containing H_3BO_3 , NaOH, KI and KIO_3 (hereafter referred as the mixed solution) and a diluted H_2SO_4 solution were prepared separately. The mixed solution and H_2SO_4 solution were injected into AFR by syringe pumps, respectively. After the system appeared stable, the reaction effluent was collected at the outlet of the reaction layer and the absorbance of the effluent at 353 nm was measured within 1 min on a UV-vis spectrophotometer (Agilent, Cary 60 UV-vis spectrophotometer). Based on the obtained concentration of I_3^- ions, the segregation index (X_s) which was defined to quantify the micromixing performance could be calculated according to the equilibrium constant of Equation 11:

$$X_s = \frac{Y}{Y_{ST}} \quad 12$$

$$Y = \frac{2(V_A + V_B)([\text{I}_2] + [\text{I}_3^-])}{V_B[\text{H}^+]_0} \quad 13$$

$$Y_{ST} = \frac{6[IO_3^-]_0}{6[IO_3^-]_0 + [H_2BO_3^-]_0} \quad 14$$

where Y denotes the ratio of the mole number of acid consumed by the Dushman reaction to the total mole number of the H^+ ions injected. Y_{ST} is the value of Y in the total segregation when the micromixing process is infinitely slow. In this case, the H^+ ions are proportionally consumed by the $H_2BO_3^-$ ions and I^-/IO_3^- ions according to their local concentrations. V_A and V_B are the volumetric flow rates of the mixed solution and H_2SO_4 solution, respectively. $[I_2]$ and $[I_3^-]$ are the concentrations of I_2 and I_3^- ions in the reaction effluent, while $[H^+]_0$ is the initial concentration of H^+ ions in H_2SO_4 solution, and $[IO_3^-]_0$ and $[H_2BO_3^-]_0$ are the initial concentrations of IO_3^- and $H_2BO_3^-$ ions in the mixed solution. The value of X_s equals to 0 for perfect mixing state, while X_s is 1 for complete segregated state. As same as Section 2.3, the effects of total flow rate and flow rate ratio were studied. According to the literature, when the flow rate ratio varied, the following equations must be fulfilled to keep the molar ratio of different ions constant [39]:

$$\frac{3V_A[IO_3^-]_0}{V_B[H^+]_0} = C_1 \quad 15$$

$$\frac{V_A[H_2BO_3^-]_0}{V_B[H^+]_0} = C_2 \quad 16$$

where C_1 and C_2 are constants. The details of the concentrations of different reactants used in this section were summarised in Table S3. The concentrations of different reactants were carefully chosen to maintain the system pH at ca. 8.5 under different process parameters to avoid the natural formation of I_2 in the absence of acid aggregates [39].

2.6 Continuous synthesis and characterisation of Ag nanoparticles (NPs)

The experimental setup for the continuous synthesis of Ag NPs is shown in Figure 4. The Ag NPs were prepared via a wet chemical method by reducing Ag^+ ions with $NaBH_4$ in the presence of Na_3CA . Na_3CA acts as a mild stabiliser which facilitates the subsequent utilisation of Ag NPs, e.g., as catalytic active sites deposited on various supports [11]. In a typical procedure, a precursor solution containing $AgNO_3$ and Na_3CA and freshly prepared $NaBH_4$ solution were separately pumped into AFR by syringe pumps. The molar ratio of Na_3CA to $AgNO_3$, and $NaBH_4$ to $AgNO_3$ were fixed at 3.5 and 6, respectively. The synthetic reaction temperature was controlled at 60 °C by a water circulator (Julabo, FP50-HE) with an external circulation connected to the heat exchanger layers. The reaction effluent flowed straight into a beaker immersed in an ice-water bath to quench the reaction and reduce the mobility and consequent

1 agglomeration of the NPs. The concentrations of AgNO₃, Na₃AC and NaBH₄ used for different
2 total flow rates and flow rate ratios were summarised in Table S4.
3
4

5
6 Figure 4 Schematic diagram of the experimental setup for the continuous synthesis of Ag NPs in the AFR.
7
8

9
10 The UV-vis spectra of the as-prepared Ag NPs were recorded on an Agilent Cary 60 UV-vis
11 spectrophotometer between 300 and 800 nm with a wavelength resolution of 0.5 nm. The
12 transmission electron microscopy (TEM) images of the as-prepared Ag NPs were acquired with
13 a FEI Tecnai TF20 FEGTEM. To avoid post-synthesis agglomeration as much as possible, the
14 specimens for TEM analysis were prepared following the protocol developed by Michen and
15 co-workers [40]. 50 µL of the as-prepared Ag NPs colloid solution and 50 µL of BSA solution
16 (0.3 mg/mL) were mixed and stored at 4 °C for 2 h prior to TEM grid preparation. A 5 µL mixture
17 droplet was dripped on the carbon copper grid (200 mesh) and then dried for 2 h naturally.
18
19

20 **3 Results and discussion**

21
22 According to LaMer model, nanoparticle formation undergoes two steps, instantaneous
23 nucleation (also known as burst nucleation) followed by diffusion controlled growth [41]. Both
24 the nucleation and growth rates, which affect the nanoparticle size and PSD, depend strongly
25 on supersaturation [42]. In a fast reaction (e.g., chemical reduction reaction in this work), the
26 supersaturation is created through mixing on the molecular scale, i.e., micromixing, which is
27 preceded by meso- and macromixing, i.e., the reduction of segregation scale controlled by fluid
28 flow. Therefore, in order to achieve a robust and controllable synthesis of NPs, the
29 understanding and control of fluid flow pattern and mixing behaviour in the reactor are of
30 theoretical and practical importance.
31
32

33
34 It is widely found that the mixing performance is strongly dependent on the process parameters
35 such as total flow rate (i.e., Reynolds number) [43, 44]. Therefore, in this study, the flow and
36 multiscale mixing behaviours under different process parameters (i.e. total flow rate and flow
37 rate ratio) were studied experimentally and numerically. Because of the limited camera
38 resolution in the flow visualisation and the assumption that the mean concentration is constant
39 on the sub-grid scales in CFD simulation, the flow visualisation and CFD simulation mainly
40 reflect the mixing process on the meso- and macroscale [45-47], while the micromixing
41
42
43
44
45
46
47
48
49
50
51
52
53
54
55
56
57
58
59
60
61
62
63
64
65

1 performance needs to be quantified by the Villermaux-Dushman method. Subsequently, the
2 relationship between the flow and multiscale mixing behaviours and the average size and PSD
3 of Ag NPs were demonstrated. Since the first three cells (the computational domain) had the
4 same geometry, it could be expected that the flow and mixing characteristics exhibited periodic
5 variation along these cells. Therefore, our following discussion mainly focused on the flow and
6 mixing behaviours in the first cell.
7
8
9
10

11 **3.1 Flow pattern and quantification of mixing performance on the meso- and macroscale** 12 **using flow visualisation and CFD simulation** 13 14

15 **3.1.1 The effect of total flow rate** 16 17

18 The MB solution entered into the reaction layer from inlet 1 and was split into two side flows
19 (S1 and S3), while the DI water was injected from inlet 2, acting as the central flow (S2). The
20 flow rate ratio was fixed at 2, while the total flow rate varied from 1 to 9 mL·min⁻¹ with the
21 Reynolds number increasing from 43 to 385. The Reynolds number was calculated based on
22 the hydraulic diameter of the nozzle (Figure 1c, 0.37 mm in width and 0.40 mm in depth).
23
24
25
26
27

28 Figure 5 shows the optical images of fluid mixing at different total flow rates. The central flow
29 of DI water was combined with two side flows of MB solution in the jet zone (hereafter referred
30 as the combined stream). For all total flow rates (1-9 mL·min⁻¹), two distinct interfaces could be
31 observed in the jet zone, indicating a laminar flow behaviour. The width of the central flow was
32 measured before the combined stream flowed into the nozzle, and the accurate position where
33 the interface between the central flow and side flow could be distinguished was marked in
34 Figure S2. As shown in Figure S2, the width of the central flow was independent of the total
35 flow rate, implying the initial MB concentration distribution across the combined stream was
36 identical at different total flow rates before flowing into the nozzle. When the total flow rate was
37 1 mL·min⁻¹ (Figure 5a), the combined stream was separated into two sub-streams once entering
38 the first cell. In each sub-stream, the DI water and MB solution flowed side by side, and no
39 disorder of the interface was observed. The interface between the water and MB solution was
40 clear even at the outlet of the first cell. This indicated that the fluid mixing was dominated by
41 molecular diffusion which was very slow under this condition. Because of the pronounced
42 inertial force at higher total flow rates, totally different flow and mixing behaviours were
43 observed at 3 mL·min⁻¹. As shown in Figure 5b, the combined stream went through the nozzle
44
45
46
47
48
49
50
51
52
53
54
55
56
57
58
59
60
61
62
63
64
65

1 along the initial flow direction and collided with the U-shaped obstacle, which split the combined
2 stream into two sub-streams. This kind of collision always created transverse motion, which
3 could increase the interfacial area for diffusion, and thus the mixing quality [48, 49]. Furthermore,
4 two symmetric expansion vortices appeared on both sides of the combined stream. The
5 generation of expansion vortices is pervasive when the cross-section of the channel is enlarged
6 abruptly, which can accelerate the mixing process by stretching and folding mechanisms [50,
7 51]. Hence, under a combination of the transverse motions caused by collision and expansion
8 vortices, no visible interface between MB solution and DI water could be seen at 3 mL·min⁻¹,
9 implying the mixing performance was much better than that at 1 mL·min⁻¹. However, darker
10 striations of MB could still be observed in the first cell at 3 mL·min⁻¹. As the total flow rate further
11 increased, the distribution of MB across the channel became more homogeneous, indicating a
12 better mixing quality. This could be attributed to the enhanced intensities of secondary flows
13 (i.e., transverse motions caused by collision and expansion vortices) with the increase in the
14 total flow rate (i.e. Reynolds number). This phenomenon is very common in the micromixers
15 with split-recombination and convergence-divergence geometries [50, 52, 53]. Besides,
16 because of the heart-shaped geometry of the cell, when the fluid flowed through the turning,
17 transverse advection, i.e., Dean vortex, caused by the gradient of the centrifugal force in the
18 cross-section of the channel might occur. Dean number (De) is defined as a control parameter
19 to predict the onset and intensity of Dean vortex, and can be calculated through the following
20 equation [54, 55]:
21
22
23
24
25
26
27
28
29
30
31
32
33
34
35
36
37
38
39

$$40 \quad De = Re \sqrt{\frac{D_h}{2R}} \quad 17$$

41 where Re represents the Reynolds number, and D_h and R are the hydraulic diameter of the
42 curved channel and the radius of curvature of the curved channel, respectively. As the total flow
43 rate increased from 1 to 9 mL·min⁻¹, Dean number increased from 7 to 60 when the fluid flowed
44 through the turning (Table S5, the Dean number was calculated based on the average radius
45 of curvature of the turning). According to the literature, when Dean number was above 20,
46 corresponding to the total flow rate of 3 mL·min⁻¹ in this study, the symmetrical vortex pair was
47 found to be formed [56, 57]. Thus, Dean vortex generated in the turning at higher total flow
48 rates could further improve the mixing quality.
49
50
51
52
53
54
55
56
57
58
59
60
61
62
63
64
65

1
2
3
4
5
6
7
8
9
10
11
12
13
14
15
16
17
18
19
20
21
22
23
24
25
26
27
28
29
30
31
32
33
34
35
36
37
38
39
40
41
42
43
44
45
46
47
48
49
50
51
52
53
54
55
56
57
58
59
60
61
62
63
64
65

Figure 5 Mixing images obtained at different total flow rates (a) 1 mL·min⁻¹, (b) 3 mL·min⁻¹, (c) 5 mL·min⁻¹, (d) 6 mL·min⁻¹, (e) 8 mL·min⁻¹, (f) 9 mL·min⁻¹ using aqueous MB solution and DI water as the working fluids when $R = 2$.

As a powerful complement to the experimental work, CFD simulation was carried out to study the effect of the total flow rate. It can offer local velocity and concentration information which cannot be obtained experimentally but is very important for deeply understanding and predicting the flow and mixing behaviours. Consistent with the flow visualisation experiments, MB solution and DI water were set to enter the reaction layer from inlets 1 and 2, respectively. To validate the CFD simulation, the numerical MB concentration distribution in the first cell was compared with that obtained from the flow visualisation, as shown in Figure 6. Because the experimental results were 2D images captured by a CCD camera for the entire channel depth, the 3D numerical results were post-processed using Tecplot 360 by averaging the MB mass fraction along the depth direction (i.e. Z-axis direction). It could be seen that the numerical results were in acceptable agreement with the experimental results.

Figure 6 Validation of CFD simulation by comparing the numerical results with the experimental results for MB concentration distribution (a, b) 1 mL·min⁻¹, (c, d) 9 mL·min⁻¹. $R = 2$, blue-white colour bar was used for comparison.

Figure 7 shows the projected particle trajectories of MB solution (blue) and DI water (red), and the contour of velocity magnitude in the X-Y plane at the middle of the channel depth ($Z = 0$) for 1 and 9 mL·min⁻¹. The flow rate ratio was maintained at 2. At 1 mL·min⁻¹, the formation of expansion vortices was not observed (Figure 7a). The combined stream was immediately split into two sub-streams once entering the first cell, in agreement with the flow visualisation. The maximum velocity of the combined stream was achieved in the nozzle (Figure 7b). After flowing into the first cell, the velocity of the combined stream decreased quickly because of stream splitting. In the case of 9 mL·min⁻¹, the difference in the projected particle trajectory was apparent compared to 1 mL·min⁻¹ (Figure 7c). Instead of splitting, the combined stream kept on flowing along the Y-axis direction until it encountered the U-shaped obstacle due to the high inertial force. This was confirmed by the contour of the velocity magnitude shown in Figure 7d.

1 The velocity of the combined stream did not decrease significantly before the stream collided
2 with the U-shaped obstacle. Expansion vortices could be observed on both sides of the
3 combined stream. The velocity magnitude of the fluid in the expansion vortex region was at a
4 very low level. Transverse motions induced by the collision and Dean vortex could be clearly
5 observed, and details are presented in Figure 8. In selected plane 1, the collision drove the fluid
6 to reverse its velocity near the obstacle. Furthermore, the turning led to a counterclockwise
7 Dean vortex in the top half of the channel (selected plane 2). The transverse motions caused
8 by the aforementioned secondary flows at higher total flow rates could promote the stretching
9 and folding of the interface, increase the interfacial area, and finally enhance the mixing
10 performance.
11
12
13
14
15
16
17
18
19
20
21

22 Figure 7 Projected particle trajectories and contour of velocity magnitude in the X-Y plane at the middle
23 of the channel depth ($Z = 0$) when (a, b) $Q_{\text{total}} = 1 \text{ mL}\cdot\text{min}^{-1}$, (c, d) $Q_{\text{total}} = 9 \text{ mL}\cdot\text{min}^{-1}$. $R = 2$.
24
25
26

27 Figure 8 Velocity vector in the selected planes coloured by velocity magnitude when $Q_{\text{total}} = 9 \text{ mL}\cdot\text{min}^{-1}$,
28 $R = 2$.
29
30
31
32

33 To quantitatively demonstrate the effect of the total flow rate on the degree of mixing, the mixing
34 index was calculated according to Equation 4. For the flow visualisation, the mixing index at the
35 outlet of the heart-shaped cell was difficult to be achieved in this study because of the existence
36 of heat exchange layers (Figure 5). Therefore, the mixing index was determined on a selected
37 plane in the sub-channel (Figure S3). As shown in Figure 9, the results of the CFD simulation
38 were in acceptable accordance with the experimental results. As the total flow rate increased
39 from 1 to 3 $\text{mL}\cdot\text{min}^{-1}$, the mixing index dramatically increased from 0.14 to 0.40. This was
40 because the mixing mechanism transformed from molecular diffusion dominated to transverse
41 advection dominated. When the total flow rate further increased from 3 to 9 $\text{mL}\cdot\text{min}^{-1}$, the mixing
42 index increased slightly from 0.40 to 0.58, which could be attributed to the higher degree of
43 transverse advection in this flow rate range.
44
45
46
47
48
49
50
51
52
53
54

55 Figure 9 Mixing index as a function of the total flow rate when $R = 2$. Equation 4 was used to calculate the
56 mixing index.
57
58
59
60
61
62
63
64
65

3.1.2 The effect of flow rate ratio

In this section, the flow rate ratio varied by changing the flow rates of MB solution and DI water while keeping the total flow rate at 9 mL·min⁻¹. As same as in Section 3.1.1, the MB solution and DI water were injected into AFR from inlets 1 and 2, respectively. The optical images of fluid mixing at different flow rate ratios are displayed in Figure 10. It could be seen that the flow rate ratio affected the initial MB concentration distribution across the combined stream in the jet zone. The width of the central flow (DI water) was measured in the same position, as shown in Figure S2. As shown in Figure 11, the width of the central flow was gradually narrowed with the increase of the flow rate ratio. As the flow rate ratio increased from 0.25 to 4, the width of the central flow decreased from 0.34 to 0.09 mm. When the flow rate ratio further increased to 8, the width of the central flow could not be distinguished due to the limited camera resolution (0.0087 mm/pixel), and particularly the fast dispersion of MB from the side flow into the central flow arising from the extremely narrow width of the central flow.

Figure 10 Mixing images obtained at different flow rate ratios (a) 0.25, (b) 0.5, (c) 1, (d) 2, (e) 4, (f) 8 using aqueous MB solution and DI water as the working fluids when $Q_{\text{total}} = 9 \text{ mL}\cdot\text{min}^{-1}$.

Figure 11 The width of the central flow in the selected position in the jet zone as a function of the flow rate ratio when $Q_{\text{total}} = 9 \text{ mL}\cdot\text{min}^{-1}$

Local flow and mixing information at different flow rate ratios were also studied by CFD simulation. The projected particle trajectories of MB solution and DI water for the flow rate ratio of 0.25, 1 and 8 are shown in Figure 12a, 12c and 12e. The symmetric expansion vortices and interweaving of the particle trajectories were clearly observed across all flow rate ratios. The evolution of the velocity profile at different flow rate ratios can be seen in Figure 12b, 12d, 12f and Figure S4. When the flow rate ratio changed, the corresponding volumetric flow rates of the streams from different inlets differed, inducing different contours of velocity magnitude in the jet zone. However, the velocity profiles of the combined streams at different flow rate ratios appeared the same once it went into the nozzle, which seemed to act as an effective microfluidic rectifier (Figure S4). Regardless of the flow rate ratio, the velocity field in the nozzle and first

1 cell was identical at a given total flow rate. Figure 13 shows the MB concentration distribution
2 in successive cross-sectional planes along the flow direction. It could be seen that the mixing
3 was dominated by molecular diffusion before the combined stream flowed into the first cell.
4 Once entering into the first cell, the mixing was enhanced by the aforementioned transverse
5 motions. As shown in Figure 13, changing the flow rate ratio affected the initial MB
6 concentration distribution across the combined stream (selected plane 1, which had the same
7 X and Y coordinates as the selected position in Figure S2). As the flow rate ratio increased, the
8 width of central flow (DI water) gradually decreased, in good accordance with the results
9 obtained in flow visualisation. In contrast, the width of side flow (MB solution) increased with
10 the increasing flow rate ratio. At the flow rate ratio of 0.25, the smallest width of the side flow
11 made the MB molecules migrate into the water most quickly. Therefore, the MB concentration
12 in the side flow decreased much faster along the flow direction at the flow rate ratio of 0.25 than
13 other flow rate ratios. Different from the spatial change of MB concentration in the side flow at
14 different flow rate ratios, the MB concentration in the central flow was changed following an
15 opposite trend. At the flow rate ratio of 0.25, nearly no MB diffused into the interior of the central
16 flow even when the combined stream reached the selected plane 5. As for the flow rate ratio of
17 8, MB could quickly diffuse across the central flow because of the narrowest width of the central
18 flow.

19
20
21
22
23
24
25
26
27
28
29
30
31
32
33
34
35
36
37
38 Figure 12 Projected particle trajectories and contour of velocity magnitude in the X-Y plane at the middle
39 of the channel depth ($Z = 0$) when (a, b) $R = 0.25$, (c, d) $R = 1$, (e, f) $R = 8$. $Q_{\text{total}} = 9 \text{ mL}\cdot\text{min}^{-1}$.

40
41
42
43
44 Figure 13 MB concentration distribution in successive cross-sectional planes along the flow direction when
45 (a) $R = 0.25$, (b) $R = 1$, (c) $R = 8$. $Q_{\text{total}} = 9 \text{ mL}\cdot\text{min}^{-1}$. The mass fraction of MB was colour-coded by the
46 colour bar.
47
48

49
50
51 The mixing indices at different flow rate ratios based on experimental and numerical results are
52 all shown in Figure 14. For the flow rate ratio of 4 and 8, the mixing indices obtained from
53 experimental results were extremely low. As mentioned in the experimental section, the mixing
54 index was calculated according to Equation 4. As shown in Table S6, the maximum standard
55 deviations of the species concentration (σ_{max}) decreased with the increasing of flow rate ratio.
56
57
58
59
60
61
62
63
64
65

1 When the flow rate ratio was 8, σ_{\max} was extremely low (0.071). In this case, the deviation of
2 the grey level caused by the non-uniform light distribution could not be ignored. At the other
3 flow rate ratios, the experimental results agreed well with CFD simulation results. Hence, the
4 effect of the flow rate ratio on the degree of mixing was discussed based on the numerical
5 results. As discussed above, when the flow rate ratio varied, σ_{\max} values also changed,
6 indicating different initial segregation states. As the flow rate ratio increased from 0.25 to 1, the
7 mixing index decreased from 0.71 to its minimum value of 0.56. When the flow rate ratio further
8 increased from 1 to 8, the mixing index increased from 0.56 to 0.70. As discussed above, the
9 obvious difference caused by changing the flow rate ratio was the initial MB concentration
10 distribution across the combined stream, while the velocity field was the same at different flow
11 rate ratios except that in the jet zone. Hence, the effect of the flow rate ratio on the degree of
12 mixing could be mainly attributed to the different initial MB concentration distributions across
13 the combined stream. This phenomenon to some extent was similar as the fact that the feed
14 position affected the mixing performance dramatically in stirred batch reactors [58]. For stirred
15 batch reactors, the stirring of the impeller always causes a nonuniform velocity field across the
16 reactor, and thus the energy dissipation rate. When the feed position is varied, the local energy
17 dissipation rates of where the feeds go into the reactor differ. This dramatically affects the
18 macromixing behaviour. For example, in the study of Assirelli et al., the difference between
19 macromixing for different feed positions was extremely obvious [54]. In this study, as discussed
20 above, the velocity field was nonuniform in AFR, and the flow rate ratio affected the initial jet
21 thickness. Hence, at different flow rate ratios, the velocity field for each stream (aqueous MB
22 solution or water) was different, which might affect the macro- and mesomixing. Different from
23 the total flow rate, the effect of the flow rate ratio on the mixing performance was rarely
24 investigated and always differed across the mixers with different structures, i.e. different mixing
25 mechanism. For example, in the study of Viktorov and co-workers, the mixing efficiencies of
26 split-and-recombination H-C mixer increased with the increase in the flow rate ratio from 1 to 3
27 [32], while Krupa and co-workers [59] claimed that the best mixing performance was obtained
28 at the flow rate ratio of 1 in a T-jet mixer. In the T-jet mixer, the mixing process was enhanced
29 by the collision between two fluids, and therefore the balancing of opposite jets was of great
30 importance.

1
2 Figure 14 The mixing index as a function of the flow rate ratio when $Q_{\text{total}} = 9 \text{ mL}\cdot\text{min}^{-1}$. Equation 4 was
3 used to calculate the mixing index.
4
5
6

7 **3.2 Quantification of the mixing performance on the microscale using Villermaux-** 8 **Dushman method** 9

10
11 Micromixing is the ultimate stage of mixing to attain molecular-scale homogeneity. The
12 environment in which micromixing takes place, e.g. the minimum scale of segregation and
13 concentration gradient, is determined by meso- and macromixing [24]. The minimum scale of
14 segregation is the outcome of mesomixing, and is the dimension within which the
15 homogenisation is achieved only by micromixing [25]. The lower the minimum scale of
16 segregation, the higher the micromixing efficiency. Because all chemical reactions occur on the
17 molecular scale, the performances of fast reactions are strongly affected by the micromixing
18 efficiency. Generally, the micromixing efficiency can be evaluated by several fast competitive
19 or consecutive reaction schemes which are sensitive to the micromixing performance [60, 61].
20 Thereinto, the Villermaux-Dushman method based on the iodide-iodate reaction system has
21 been widely employed to assess the overall micromixing efficiencies of various mixers [39, 62].
22 In this section, sulphuric acid solution was injected into the reaction layer from inlet 1, while the
23 mixed solution containing H_2BO_3^- , I^- and IO_3^- was injected from inlet 2, acting as the central flow.
24 Figure 15a shows the plot of the segregation index as a function of the total flow rate with the
25 flow rate ratio of 2, and the concentration of different ions kept constant. When the total flow
26 rate was $1 \text{ mL}\cdot\text{min}^{-1}$, the segregation index was as high as 0.038, indicating a poor micromixing
27 efficiency. As discussed in Section 3.1.1, the mixed solution and sulphuric acid solution flowed
28 side by side at $1 \text{ mL}\cdot\text{min}^{-1}$. Hence, the competitive reaction system occurred at the interface
29 between two reactant streams and was controlled by molecular diffusion. Initially, H^+ ions were
30 consumed preferentially by H_2BO_3^- ions at the interface, and the formation of I_2 was very limited.
31 However, along the flow direction, the unreacted I^- and IO_3^- ions at the interface gradually
32 diffused into the sulphuric acid solution, leading to the formation of a large amount of I_3^- ions,
33 and thus a high segregation index. As the total flow rate increased from 1 to $6 \text{ mL}\cdot\text{min}^{-1}$, the
34 segregation index decreased significantly from 0.038 to 0.0037. This indicated that better
35 micromixing performances could be achieved at higher total flow rates. With the further increase
36
37
38
39
40
41
42
43
44
45
46
47
48
49
50
51
52
53
54
55
56
57
58
59
60
61
62
63
64
65

1 of the total flow rate, only a slight decrease in the segregation index was observed, implying
2 the enhancement effect of the evaluated total flow rate on micromixing was not pronounced
3 over 6 mL·min⁻¹. It was evident that the total flow rate showed the same effect on the
4 micromixing performance as that on the meso- and macromixing performance (quantified by
5 the mixing index in Section 3.1.1). This was because that increasing the total flow rate
6 enhanced the intensities of the secondary flows, leading to an improved meso- and
7 macromixing. A better meso- and macromixing performance could offer a more uniform
8 concentration distribution, which could inhibit the occurrence of Dushman reaction.
9 Furthermore, the enhanced secondary flows could reduce the minimum scale of segregation to
10 a large extent, which facilitated the mixing on the microscale.
11
12
13
14
15
16
17
18
19
20
21

22 Figure 15 Plots of segregation index (XS) and micromixing time as a function of (a, c) total flow rate, R =
23 2, (b, d) flow rate ratio, Q_{total} = 9 mL·min⁻¹.
24
25
26
27

28 Figure 15b shows the effect of the flow rate ratio on the segregation index. The segregation
29 index decreased from 0.014 to 0.0016 as the flow rate ratio increased from 0.25 to 2. As the
30 flow rate ratio further increased from 2 to 8, no obvious change in the segregation index was
31 observed. Different from the situation when the total flow rate varied, the effect of the flow rate
32 ratio on the segregation index was different from that of the flow rate ratio on the mixing index.
33
34 Initially, Villermaux-Dushman method was widely used for evaluating the mixing performances
35 of batch reactors. When this method was implemented to the continuous reactor, Equation 15
36 and 16 must be satisfied at different flow rate ratios. In other words, the molar ratio of different
37 ions should be kept unchanged. Hence, the initial concentration of H⁺ ions should increase with
38 the decrease in the flow rate of sulphuric acid solution. It has been reported that the Dushman
39 reaction was more sensitive to the concentration of H⁺ ions compared to the neutralisation of
40 H₂BO₃⁻ [63, 64]. Kölbl and co-workers found that the absorption of I₃⁻ (i.e. segregation index)
41 increased with the increasing concentration of H⁺ ions because the local reaction rate was
42 determined by the local concentrations of the reactants and the Dushman reaction mainly
43 happened in H⁺ ions-rich region [65]. For microreactors, when studying the effect of flow rate
44 ratio, the segregation index was widely found to decrease with the increasing flow rate of
45 sulphuric acid solution (i.e. the decreasing initial concentration of H⁺ ions) [66]. Similar to the
46
47
48
49
50
51
52
53
54
55
56
57
58
59
60
61
62
63
64
65

1 previous studies, as shown in Figure 15b, the segregation index was determined by the initial
2 concentration of H⁺ ions in this study. As shown in CFD simulation, the difference in the mixing
3 indices at different flow rate ratios was within 15%. It could be deduced the local concentration
4 of H⁺ ions in the in H⁺ ions-rich region was higher when the initial concentration of H⁺ ions was
5 larger. When the flow rate ratio was 0.25, the initial H⁺ concentration was as high as 0.12 M,
6 leading to the maximum value of the segregation index. When the flow rate ratio increased from
7 2 to 8, there was only a slight increase in the initial concentration of H⁺ ions, so the segregation
8 showed no obvious change. Therefore, when the flow rate ratio changed, many factors
9 including the multiscale mixing performance and initial concentration of reactants, might affect
10 the final reaction behaviour.
11

12 As shown in the aforementioned results, besides the micromixing performance, the segregation
13 index was highly dependent on the reactant concentration. This dependency made a
14 comparison between different studies difficult. Therefore, the micromixing time, which was
15 independent of the reactant concentration, was needed to be extracted from the experimental
16 results. Up to now, several models such as inter exchange with the mean (IEM) model [67],
17 incorporation model [45, 68] and engulfment deformation diffusion (EDD) model [69] have been
18 proposed to describe the mixing process. In this study, the micromixing time was estimated by
19 the incorporation model. More details about incorporation model could be seen in the study of
20 Yang and co-workers [68]. With a series of presumed value of micromixing time and known
21 initial concentration of different ions in each solution, the ordinary differential equations (see
22 the details in the supplementary material) could be solved by MATLAB (ode15s). The value of
23 time step was fixed at 10⁻⁸ s, and the integration process was terminated when the H⁺ ions were
24 completely consumed with 10⁻⁸ M as the criterion. The calculated relationship between the
25 micromixing time and segregation index was shown in Figure S5. Figure 15c and Figure 15d
26 depict the effects of the total flow rate and flow rate ratio on the micromixing time. It is worth
27 noting that the mechanism for micromixing is very complex, but the aforementioned models are
28 all highly simplified. Therefore, the micromixing time estimations obtained from these models
29 can only give reliable orders of magnitude rather than the accurate values. Falk and Commenge
30 claimed that the accuracy of micromixing time determination from IEM model could not be better
31 than ± 30%, and for example, all mixing time values between 0.13 and 0.07 s could be
32

1 considered as equal to 0.1 s [70]. As shown in Figure 15c, the micromixing time decreased
2 from 0.17 to 0.004 s as the total flow rate increased from 1 to 9 mL·min⁻¹. For all flow rate ratios,
3 the micromixing time fluctuated around 0.005 s. Considering the accuracy of the model, it could
4 be concluded that the micromixing times obtained at different flow rate ratios were in the same
5 order of magnitude (Figure 15d). As mentioned above, the micromixing occurred on the
6 minimum scale of segregation, which was determined by the intensities of secondary flows. As
7 discussed in Section 3.1.2, in the first cell where transverse motions happened, the velocity
8 field was the same at different flow rate ratios. It could be expected that the minimum scale of
9 segregation was identical at different flow rate ratios. Therefore, it was reasonable that the
10 micromixing time was nearly independent of the flow rate ratio.

21 **3.3. Continuous synthesis of the Ag NPs**

22 Based on the above discussion, an adequate understanding of the flow and mixing
23 characteristics in AFR has been obtained. In this section, the performance of AFR for the
24 continuous synthesis of nanomaterials was evaluated, with most attention paid to how the flow
25 and multiscale mixing characteristics affected the average particle size and PSD. Because of
26 the diverse morphologies and intriguing size/morphology-dependent properties of Ag NPs, the
27 continuous synthesis of Ag NPs was employed as the model system in AFR. In fact, Ag NPs
28 have been widely synthesised in a continuous manner [4, 71, 72]. The particle size of Ag NPs
29 was found to be closely related to the micromixing performance [4, 11, 73]. Better micromixing
30 leads to more uniform and higher local supersaturation, and thus smaller average particle size
31 and narrower PSD. The aforementioned results showed that the total flow rate and flow rate
32 ratio had significant effects on the flow and mixing characteristics, so it could be anticipated
33 that these two parameters affected as well the average particle size and PSD of Ag NPs.

34 In this section, NaBH₄ solution was injected into AFR from inlet 1 (side flow), while the Ag
35 precursor solution was injected into the AFR from inlet 2 (central flow). First, the effect of the
36 total flow rate was studied. The total flow rate varied from 1 to 9 mL·min⁻¹, while the flow rate
37 ratio was maintained at 2. Figure 16a shows the UV-vis absorption spectra of Ag NPs
38 synthesised at different total flow rates. As is well known, the PSD of as-prepared Ag NPs can
39 be deduced by the full width at half maximum (FWHM) [74]. Generally, the larger the FWHM,
40 the wider the PSD. The UV-vis absorption spectra of Ag NPs synthesised at low total flow rates

(1 mL·min⁻¹) exhibited an asymmetric shape, i.e. a main peak at ca. 388 nm and a shoulder peak at ca. 410 nm, both of which could be assigned to the characteristic absorption peak of spherical-like Ag NPs [75]. As the total flow rate increased from 1 to 9 mL·min⁻¹, the shoulder peak gradually disappeared, along with the FWHM decreasing from 65 to 52 nm (Figure 16b), implying a narrower PSD of Ag NPs. Figure 16c and Figure 16d show the TEM images and corresponding PSD of Ag NPs synthesised at 1 and 9 mL·min⁻¹. Both samples exhibited a sphere-like morphology. The average particle sizes of Ag NPs synthesised at 1 and 9 mL·min⁻¹ were 7.2 ± 3.9 and 4.6 ± 1.8 nm, respectively. The Ag NPs synthesised at 1 mL·min⁻¹ showed a bimodal PSD (one peak centred at 2.8 nm, and the other centred at 10.1 nm), which was much broader than that of Ag NPs synthesised at 9 mL·min⁻¹, agreeing with the UV-vis absorption spectra. This indicated that increasing the total flow rate could reduce the average particle size and narrow the PSD of Ag NPs. Taking the results obtained in flow visualisation, CFD simulation and Villermaux-Dushman reaction system into consideration, the effect of the total flow rate could be merely attributed to the change in micromixing performance. The worst micromixing performance at 1 mL·min⁻¹ induced the largest average particle size and widest PSD. As discussed above, Ag NPs are formed by burst nucleation through LaMer mechanism, followed by further growth via diffusion growth, Ostwald ripening or coalescence [76]. At 1 mL·min⁻¹, the NaBH₄ solution and Ag precursor solution flowed side by side. The reduction reaction occurred at the interface between these two flows in the beginning. When the supersaturation of Ag monomer exceeded the critical value, nuclei were formed. As the molecular diffusion proceeded, both homogenous nucleation and heterogeneous nucleation with already existing nuclei as the nucleation sites might happen. The nuclei generated at different positions along the flow direction experienced different growth histories, leading to a wide and bimodal PSD. When the total flow rate increased, the micromixing performance became better, thereby leading to a smaller average particle size and narrower PSD.

Figure 16 (a) UV-vis absorption spectra of Ag NPs synthesised at different total flow rates, (b) FWHM as a function of the total flow rate, TEM images and particle size distribution of Ag NPs synthesised at (c) 1 mL·min⁻¹ and (d) 9 mL·min⁻¹ when $R = 2$. The line is given as eye guide only.

In line with the above experiments, the flow rate ratio varied from 0.25 to 8, while the total flow

1 rate was kept at 9 mL·min⁻¹ in this section. Figure 17a shows the UV-vis absorption spectra of
2 Ag NPs synthesised at different flow rate ratios. As the flow rate ratio increased from 0.25 to 8,
3 the FWHM decreased from 70 to 49 nm (Figure 17b). This implied that the Ag NPs synthesised
4 at a higher flow rate ratio had a narrower PSD. This was further confirmed by the results of
5 TEM characterisation (Figure 17c and 17d). The average particle sizes of Ag NPs synthesised
6 at 0.25 and 8 were 7.5 ± 3.9 and 4.3 ± 1.8 nm, respectively. Evidently, when the flow rate ratio
7 varied, the PSD of Ag NPs did not change following the same trend as the mixing index (meso-
8 and macromixing performance) and micromixing time (micromixing performance). In this
9 section, the molar ratios between NaBH₄ and AgNO₃, and Na₃AC and AgNO₃ were maintained
10 at 6 and 3, respectively. According to the literature, Ag⁺ ions reacted with BH₄⁻ ions under the
11 basic environment via the following equation [4]:
12



14 It was apparent that a large excess of NaBH₄ was used in this section. As discussed in flow
15 visualisation and CFD simulation, the central flow exhibited the largest width at the flow rate
16 ratio of 0.25. As depicted in Figure 13, only a minor amount of MB from the side flow diffused
17 into the interior of the central flow in the selected plane 5. Even when the fluid arrived at the
18 selected plane 6, the MB concentration in the area marked with a black rectangle was still at a
19 very low level (Figure S6). Therefore, it could be predicted that the diffusion of BH₄⁻ ions from
20 the side flow (NaBH₄ solution) into the interior of the central flow (Ag precursor solution), or the
21 diffusion of Ag⁺ ions from the interior of the central flow to the side flow required a longer time
22 at the flow rate ratio of 0.25, as compared to other flow rate ratios. In this case, the nucleation
23 of Ag NPs kept happening for a longer duration along the flow direction until Ag⁺ ions were
24 completely consumed. As a result, Ag NPs with a broader PSD were obtained at the flow rate
25 ratio of 0.25. At the flow rate ratio of 8, the width of the Ag precursor stream was the narrowest,
26 so BH₄⁻ could migrate quickly across the Ag precursor stream. Before perfect mixing was
27 achieved, most of Ag⁺ ions could be reduced in a short period, because excessive NaBH₄ was
28 used. Consequently, a narrower PSD was obtained at the flow rate ratio of 8 as compared to
29 0.25. These observations confirmed previous findings that the width of the central flow affected
30 the average particle size and morphology of nanomaterials. For example, when using 3D
31 hydrodynamic focusing, Lu and co-workers reported that while changing the flow rate of the
32

1 side flow, the outer profile of the central flow and the molar ratio of two reactants varied, leading
2 to the formation of Au hybrid materials with different morphologies [77]. Jahn and co-workers
3 found the hydrodynamically focused width of alcohol stream (central flow) strongly influenced
4 the vesicle size distributions in microfluidic hydrodynamic focusing system [78].
5
6
7
8
9

10 Figure 17 (a) UV-vis absorption spectra of Ag NPs synthesised at different flow rate ratios, (b) FWHM as
11 a function of the flow rate ratio, TEM images and particle size distributions of Ag NPs synthesised at the
12 flow rate ratio of (c) 0.25 and (d) 8 when $Q_{\text{total}} = 9 \text{ mL}\cdot\text{min}^{-1}$. The line is given as eye guide only.
13
14
15
16
17

18 **4 Conclusion**

19 First, the flow and mixing characteristics (mainly on the meso- and macroscale) of two miscible
20 liquids in Corning AFR Lab Reactor module were studied by the flow visualisation and 3D CFD
21 simulation with the MB solution and DI water as the working fluids. The results showed that the
22 CFD simulation agreed well with the experiments. It was found that the total flow rate (1-9
23 $\text{mL}\cdot\text{min}^{-1}$) and flow rate ratio (0.25-8) both significantly affected the flow and mixing
24 characteristics. With the increase in the total flow rate, a flow pattern evolution from laminar
25 flow ($1 \text{ mL}\cdot\text{min}^{-1}$) to a complex flow containing transverse advection ($3-9 \text{ mL}\cdot\text{min}^{-1}$) was
26 observed. The mixing index increased with the increase in the total flow rate, indicating a better
27 mixing performance. The improved mixing performance at evaluated total flow rate could be
28 attributed to the enhanced secondary flows (i.e. transverse motion caused by the collision with
29 the U-shaped obstacle, expansion vortices and Dean vortices) originating from the unique
30 structural feature of AFR. As for the flow rate ratio, it affected the widths of the central and side
31 flows in the jet zone, i.e. initial concentration distribution profile across the combined stream,
32 thereby inducing different mixing performances. The best mixing performance was obtained at
33 the flow rate ratio of 0.25 and 8.
34
35
36
37
38
39
40
41
42
43
44
45
46
47
48
49

50 Subsequently, the micromixing efficiency which strongly affected the reaction performance was
51 studied by the Villermaux-Dushman method. The segregation index as well as the micromixing
52 time decreased with the increase of the total flow rate, implying a better micromixing efficiency.
53 The flow rate ratio affected the segregation index in a complex manner. Across the flow rate
54 ratio studied, the micromixing times were in the same order of magnitude. When the continuous
55
56
57
58
59
60
61
62
63
64
65

1 synthesis of Ag NPs was carried out, a similar phenomenon was observed. As the total flow
2 rate increased, the PSD of Ag NPs became narrower due to the better micromixing efficiency
3 at higher total flow rates. When the flow rate ratio changed, the PSD of Ag NPs was dependent
4 on the width of the Ag precursor solution. To sum up, the aforementioned results provide a
5 deeper understanding of the flow and mixing characteristics, and their effects on the PSD of Ag
6 NPs in a Coning AFR. It will pave the way for large scale production of size-tunable Ag NPs in
7 our future work.
8
9
10
11
12
13

14 **Acknowledgements**

15 K.W. and R.B. acknowledge financial support from the Engineering and Physical Sciences
16 Research Council Impact Acceleration Account (EPSRC, EP/R511717/1). We thank Corning
17 SAS for donating the AFR module. J.Z. acknowledges the Fundamental Research Funds for
18 the Central Universities (3132020168). L.Y. acknowledges financial support from the China
19 Scholarship Council (CSC) (Grant No. 201909110122). T.B. acknowledges financial support
20 from EPSRC Doctoral Training Partnership (DTP).
21
22
23
24
25
26
27
28
29
30
31
32
33

34 **References**

- 35
36 [1] Y.N. Xia, Are We Entering the Nano Era?, *Angewandte Chemie-International Edition* 53
37 (2014) 12268-12271.
38
39 [2] A matter of scale, *Nature Nanotechnology* 11 (2016) 733-733.
40
41 [3] R.L.M. Robinson, I. Lynch, W. Peijnenburg, J. Rumble, F. Klaessig, C. Marquardt, H.
42 Rauscher, T. Puzyn, R. Purian, C. Aberg, S. Karcher, H. Vriens, P. Hoet, M.D. Hoover, C.O.
43 Hendren, S.L. Harper, How should the completeness and quality of curated nanomaterial data
44 be evaluated?, *Nanoscale* 8 (2016) 9919-9943.
45
46 [4] K.J. Wu, L. Torrente-Murciano, Continuous synthesis of tuneable sized silver nanoparticles
47 via a tandem seed-mediated method in coiled flow inverter reactors, *Reaction Chemistry &*
48 *Engineering* 3 (2018) 267-276.
49
50 [5] H. Huang, H. du Toit, M.O. Besenhard, S. Ben-Jaber, P. Dobson, I. Parkin, A. Gavriilidis,
51 Continuous flow synthesis of ultrasmall gold nanoparticles in a microreactor using trisodium
52 citrate and their SERS performance, *Chemical Engineering Science* 189 (2018) 422-430.
53
54 [6] X.L. Huang, L.L. Li, T.L. Liu, N.J. Hao, H.Y. Liu, D. Chen, F.Q. Tang, The Shape Effect of
55 Mesoporous Silica Nanoparticles on Biodistribution, Clearance, and Biocompatibility in Vivo,
56 *Acs Nano* 5 (2011) 5390-5399.
57
58
59
60
61
62
63
64
65

- 1 [7] F.M. Akwi, P. Watts, Continuous flow chemistry: where are we now? Recent applications,
2 challenges and limitations, *Chemical Communications* 54 (2018) 13894-13928.
- 3 [8] G.Y. Lin, S. Jiang, C.Y. Zhu, T.T. Fu, Y.G. Ma, Mass-Transfer Characteristics of CO₂
4 Absorption into Aqueous Solutions of N-Methyldiethanolamine plus Diethanolamine in a T-
5 Junction Microchannel, *Acs Sustainable Chemistry & Engineering* 7 (2019) 4368-4375.
- 6 [9] W.Z. Guo, H.J. Heeres, J. Yue, Continuous synthesis of 5-hydroxymethylfurfural from
7 glucose using a combination of AlCl₃ and HCl as catalyst in a biphasic slug flow capillary
8 microreactor, *Chemical Engineering Journal* 381 (2020).
- 9 [10] H.Y. Ma, N. Jin, P. Zhang, Y.F. Zhou, Y.C. Zhao, X.L. Zhang, H.Y. Lu, J. Liu, Dynamic
10 characterization of nanoparticles production in a droplet-based continuous flow microreactor,
11 *Chemical Engineering Research & Design* 144 (2019) 247-257.
- 12 [11] S. Tao, M. Yang, H.H. Chen, G.W. Chen, Continuous Synthesis of Highly Uniform Noble
13 Metal Nanoparticles over Reduced Graphene Oxide Using Microreactor Technology, *Acs*
14 *Sustainable Chemistry & Engineering* 6 (2018) 8719-8726.
- 15 [12] K.J. Wu, Y.H. Gao, L. Torrente-Murciano, Continuous synthesis of hollow silver-palladium
16 nanoparticles for catalytic applications, *Faraday Discussions* 208 (2018) 427-441.
- 17 [13] L. Panariello, S. Damilos, H. du Toit, G.W. Wu, A.N.P. Radhakrishnan, I.P. Parkin, A.
18 Gavriilidis, Highly reproducible, high-yield flow synthesis of gold nanoparticles based on a
19 rational reactor design exploiting the reduction of passivated Au(III), *Reaction Chemistry &*
20 *Engineering* 5 (2020) 663-676.
- 21 [14] X.X. Liang, R.W. Baker, K.J. Wu, W.T. Deng, D. Ferdani, P.S. Kubiak, F. Marken, L.
22 Torrente-Murciano, P.J. Cameron, Continuous low temperature synthesis of MAPbX₃
23 perovskite nanocrystals in a flow reactor, *Reaction Chemistry & Engineering* 3 (2018) 640-644.
- 24 [15] J.B. Wacker, I. Lignos, V.K. Parashar, M.A.M. Gijs, Controlled synthesis of fluorescent
25 silica nanoparticles inside microfluidic droplets, *Lab on a Chip* 12 (2012) 3111-3116.
- 26 [16] C. Echaide-Gorritz, C. Clement, F. Cacho-Bailo, C. Tellez, J. Coronas, New strategies
27 based on microfluidics for the synthesis of metal-organic frameworks and their membranes,
28 *Journal of Materials Chemistry A* 6 (2018) 5485-5506.
- 29 [17] M. Qiu, L. Zha, Y. Song, L. Xiang, Y.H. Su, Numbering-up of capillary microreactors for
30 homogeneous processes and its application in free radical polymerization, *Reaction Chemistry*
31 *& Engineering* 4 (2019) 351-361.
- 32 [18] E. Rossi, P. Woehl, M. Maggini, Scalable in Situ Diazomethane Generation in Continuous-
33 Flow Reactors, *Organic Process Research & Development* 16 (2012) 1146-1149.
- 34 [19] Y.J. Zhang, S.C. Born, K.F. Jensen, Scale-Up Investigation of the Continuous Phase-
35 Transfer-Catalyzed Hypochlorite Oxidation of Alcohols and Aldehydes, *Organic Process*
36 *Research & Development* 18 (2014) 1476-1481.
- 37 [20] C. Penverne, B. Hazard, C. Rolando, M. Penhoat, Scale-up Study of Benzoic Acid
38 Alkylation in Flow: From Microflow Capillary Reactor to a Milliflow Reactor, *Organic Process*
39 *Research & Development* 21 (2017) 1864-1868.
- 40
41
42
43
44
45
46
47
48
49
50
51
52
53
54
55
56
57
58
59
60
61
62
63
64
65

- 1 [21] U. Novak, D. Lavric, P. Znidarsic-Plazl, Continuous Lipase B-Catalyzed Isoamyl Acetate
2 Synthesis in a Two-Liquid Phase System Using Corning (R) AFR (TM) Module Coupled with a
3 Membrane Separator Enabling Biocatalyst Recycle, *Journal of Flow Chemistry* 6 (2016) 33-38.
- 4 [22] A. Roibu, C. Horn, T. Van Gerven, S. Kuhn, Photon Transport and Hydrodynamics in Gas-
5 Liquid Flows. Part 2: Characterization of Bubbly Flow in an Advanced-Flow Reactor,
6 *ChemPhotoChem*.
- 7 [23] P. Bianchi, G. Petit, J.-C.M. Monbaliu, Scalable and robust photochemical flow process
8 towards small spherical gold nanoparticles, *Reaction Chemistry & Engineering* (2020).
- 9 [24] B.K. Johnson, R.K. Prud'homme, Chemical processing and micromixing in confined
10 impinging jets, *AIChE Journal* 49 (2003) 2264-2282.
- 11 [25] X.Y. Lin, J.S. Zhang, K. Wang, G.S. Luo, Determination of the Micromixing Scale in a
12 Microdevice by Numerical Simulation and Experiments, *Chemical Engineering & Technology*
13 39 (2016) 909-917.
- 14 [26] R. Gerardy, J. Estager, P. Luis, D.P. Debecker, J.C. Monbaliu, Versatile and scalable
15 synthesis of cyclic organic carbonates under organocatalytic continuous flow conditions,
16 *Catalysis Science & Technology* 9 (2019) 6841-6851.
- 17 [27] M. Peer, N. Weeranoppanant, A. Adamo, Y.J. Zhang, K.F. Jensen, Biphasic Catalytic
18 Hydrogen Peroxide Oxidation of Alcohols in Flow: Scale-up and Extraction, *Organic Process*
19 *Research & Development* 20 (2016) 1677-1685.
- 20 [28] S.H. Wong, M.C.L. Ward, C.W. Wharton, Micro T-mixer as a rapid mixing micromixer,
21 *Sensors and Actuators B-Chemical* 100 (2004) 359-379.
- 22 [29] C.Y. Wu, R.T. Tsai, Fluid mixing via multidirectional vortices in converging-diverging
23 meandering microchannels with semi-elliptical side walls, *Chemical Engineering Journal* 217
24 (2013) 320-328.
- 25 [30] I. Shah, S.W. Kim, K. Kim, Y.H. Doh, K.H. Choi, Experimental and numerical analysis of
26 Y-shaped split and recombination micro-mixer with different mixing units, *Chemical Engineering*
27 *Journal* 358 (2019) 691-706.
- 28 [31] M. Bayareh, M.N. Ashani, A. Usefian, Active and passive micromixers: A comprehensive
29 review, *Chemical Engineering and Processing-Process Intensification* 147 (2020).
- 30 [32] V. Viktorov, M.R. Mahmud, C. Visconte, Numerical study of fluid mixing at different inlet
31 flow-rate ratios in Tear-drop and Chain micromixers compared to a new H-C passive
32 micromixer, *Engineering Applications of Computational Fluid Mechanics* 10 (2016) 183-193.
- 33 [33] S. Sarkar, K.K. Singh, V. Shankar, K.T. Shenoy, Numerical simulation of mixing at 1-1 and
34 1-2 microfluidic junctions, *Chemical Engineering and Processing-Process Intensification* 85
35 (2014) 227-240.
- 36 [34] K.J. Wu, V. Nappo, S. Kuhn, Hydrodynamic Study of Single- and Two-Phase Flow in an
37 AdvancedFlow Reactor, *Industrial & Engineering Chemistry Research* 54 (2015) 7554-7564.
- 38 [35] A.A. Selifonov, O.G. Shapoval, A.N. Mikerov, V.V. Tuchin, Determination of the Diffusion
39 Coefficient of Methylene Blue Solutions in Dentin of a Human Tooth using Reflectance
40
41
42
43
44
45
46
47
48
49
50
51
52
53
54
55
56
57
58
59
60
61
62
63
64
65

Spectroscopy and Their Antibacterial Activity during Laser Exposure, Optics and Spectroscopy 126 (2019) 758-768.

[36] M. Sadegh Cheri, H. Latifi, M. Salehi Moghaddam, H. Shahraki, Simulation and experimental investigation of planar micromixers with short-mixing-length, Chemical Engineering Journal 234 (2013) 247-255.

[37] Y.H. Su, G.W. Chen, Q. Yuan, Influence of hydrodynamics on liquid mixing during Taylor flow in a microchannel, AIChE Journal 58 (2012) 1660-1670.

[38] M.C. Fournier, L. Falk, J. Villermaux, A new parallel competing reaction system for assessing micromixing efficiency—Experimental approach, Chemical Engineering Science 51 (1996) 5053-5064.

[39] P. Guichardon, L. Falk, Characterisation of micromixing efficiency by the iodide-iodate reaction system. Part I: experimental procedure, Chemical Engineering Science 55 (2000) 4233-4243.

[40] B. Michen, C. Geers, D. Vanhecke, C. Endes, B. Rothen-Rutishauser, S. Balog, A. Petri-Fink, Avoiding drying-artifacts in transmission electron microscopy: Characterizing the size and colloidal state of nanoparticles, Scientific Reports 5 (2015).

[41] V.K. Lamer, R.H. Dinegar, THEORY, PRODUCTION AND MECHANISM OF FORMATION OF MONODISPERSED HYDROSOLS, Journal of the American Chemical Society 72 (1950) 4847-4854.

[42] H.C. Schwarzer, W. Peukert, Tailoring particle size through nanoparticle precipitation, Chemical Engineering Communications 191 (2004) 580-606.

[43] T.L. Xie, C. Xu, Numerical and experimental investigations of chaotic mixing behavior in an oscillating feedback micromixer, Chemical Engineering Science 171 (2017) 303-317.

[44] V. Mengeaud, J. Josserand, H.H. Girault, Mixing processes in a zigzag microchannel: Finite element simulations and optical study, Analytical Chemistry 74 (2002) 4279-4286.

[45] Y.H. Su, G.W. Chen, Q. Yuan, Ideal micromixing performance in packed microchannels, Chemical Engineering Science 66 (2011) 2912-2919.

[46] D.L. Marchisio, A.A. Barresi, CFD simulation of mixing and reaction: the relevance of the micro-mixing model, Chemical Engineering Science 58 (2003) 3579-3587.

[47] R.O. Fox, On the relationship between Lagrangian micromixing models and computational fluid dynamics, Chemical Engineering and Processing-Process Intensification 37 (1998) 521-535.

[48] J.B. You, Y. Choi, S.G. Im, Influence of adjusting the inlet channel confluence angle on mixing behaviour in inertial microfluidic mixers, Microfluidics and Nanofluidics 21 (2017).

[49] M.A. Ansari, K.Y. Kim, K. Anwar, S.M. Kim, A novel passive micromixer based on unbalanced splits and collisions of fluid streams, Journal of Micromechanics and Microengineering 20 (2010).

[50] M.K. Parsa, F. Hormozi, Experimental and CFD modeling of fluid mixing in sinusoidal microchannels with different phase shift between side walls, Journal of Micromechanics and Microengineering 24 (2014).

- 1 [51] C. Liu, Y. Li, Y.W. Li, P. Chen, X.J. Feng, W. Du, B.F. Liu, Rapid three-dimensional
2 microfluidic mixer for high viscosity solutions to unravel earlier folding kinetics of G-quadruplex
3 under molecular crowding conditions, *Talanta* 149 (2016) 237-243.
- 4 [52] M.A. Ansari, K.Y. Kim, A Numerical Study of Mixing in a Microchannel with Circular Mixing
5 Chambers, *AIChE Journal* 55 (2009) 2217-2225.
- 6 [53] M.S. Cheri, H. Latifi, M.S. Moghaddam, H. Shahraki, Simulation and experimental
7 investigation of planar micromixers with short-mixing-length, *Chemical Engineering Journal* 234
8 (2013) 247-255.
- 9 [54] W.R. Dean, The stream-line motion of fluid in a curved pipe. (Second paper.), *Philosophical*
10 *Magazine* 5 (1928) 673-695.
- 11 [55] K.C. Cheng, M. Akiyama, LAMINAR FORCED CONVECTION HEAT TRANSFER IN
12 CURVED RECTANGULAR CHANNELS, *International Journal of Heat and Mass Transfer* 13
13 (1970) 471-&.
- 14 [56] A.A. Mouza, C.M. Patsa, F. Schonfeld, Mixing performance of a chaotic micro-mixer,
15 *Chemical Engineering Research & Design* 86 (2008) 1128-1134.
- 16 [57] N. Nivedita, P. Ligrani, I. Papautsky, Dean Flow Dynamics in Low-Aspect Ratio Spiral
17 Microchannels, *Scientific Reports* 7 (2017).
- 18 [58] M. Assirelli, W. Bujalski, A. Eaglesham, A.W. Nienow, Macro- and micromixing studies in
19 an unbaffled vessel agitated by a Rushton turbine, *Chemical Engineering Science* 63 (2008)
20 35-46.
- 21 [59] K. Krupa, M.A. Sultan, C.P. Fonte, M.I. Nunes, M.M. Dias, J.C.B. Lopes, R.J. Santos,
22 Characterization of mixing in T-jets mixers, *Chemical Engineering Journal* 207 (2012) 931-937.
- 23 [60] Y. Song, M.J. Shang, G.X. Li, Z.H. Luo, Y.H. Su, Influence of Mixing Performance on
24 Polymerization of Acrylamide in Capillary Microreactors, *AIChE Journal* 64 (2018) 1828-1840.
- 25 [61] K. Kunowa, S. Schmidt-Lehr, W. Pauer, H.U. Moritz, C. Schwede, Characterization of
26 mixing efficiency in polymerization reactors using competitive-parallel reactions,
27 *Macromolecular Symposia* 259 (2007) 32-41.
- 28 [62] M.C. Fournier, L. Falk, J. Villermaux, A new parallel competing reaction system for
29 assessing micromixing efficiency - Determination of micromixing time by a simple mixing model,
30 *Chemical Engineering Science* 51 (1996) 5187-5192.
- 31 [63] A. Kolbl, S. Schmidt-Lehr, The iodide iodate reaction method: The choice of the acid,
32 *Chemical Engineering Science* 65 (2010) 1897-1901.
- 33 [64] Q.A. Wang, J.X. Wang, W. Yu, L. Shao, G.Z. Chen, J.F. Chen, Investigation of Micromixing
34 Efficiency in a Novel High-Throughput Microporous Tube-in-Tube Microchannel Reactor,
35 *Industrial & Engineering Chemistry Research* 48 (2009) 5004-5009.
- 36 [65] A. Kolbl, V. Desplantes, L. Grundemann, S. Scholl, Kinetic investigation of the Dushman
37 reaction at concentrations relevant to mixing studies in stirred tank reactors, *Chemical*
38 *Engineering Science* 93 (2013) 47-54.
- 39 [66] M.Z. Guo, X.J. Hu, F. Yang, S. Jiao, Y.J. Wang, H.Y. Zhao, G.S. Luo, H.M. Yu, Mixing
40 Performance and Application of a Three-Dimensional Serpentine Microchannel Reactor with a
41
42
43
44
45
46
47
48
49
50
51
52
53
54
55
56
57
58
59
60
61
62
63
64
65

1
2
3
4
5
6
7
8
9
10
11
12
13
14
15
16
17
18
19
20
21
22
23
24
25
26
27
28
29
30
31
32
33
34
35
36
37
38
39
40
41
42
43
44
45
46
47
48
49
50
51
52
53
54
55
56
57
58
59
60
61
62
63
64
65

Periodic Vortex-Inducing Structure, *Industrial & Engineering Chemistry Research* 58 (2019) 13357-13365.

[67] J.M. Commenge, L. Falk, Villermaux-Dushman protocol for experimental characterization of micromixers, *Chemical Engineering and Processing-Process Intensification* 50 (2011) 979-990.

[68] H.J. Yang, G.W. Chu, J.W. Zhang, Z.G. Shen, J.F. Chen, Micromixing efficiency in a rotating packed bed: Experiments and simulation, *Industrial & Engineering Chemistry Research* 44 (2005) 7730-7737.

[69] A. Nie, Z.M. Gao, L. Xue, Z.Q. Cai, G.M. Evans, A. Eaglesham, Micromixing performance and the modeling of a confined impinging jet reactor/high speed disperser, *Chemical Engineering Science* 184 (2018) 14-24.

[70] L. Falk, J.M. Commenge, Performance comparison of micromixers, *Chemical Engineering Science* 65 (2010) 405-411.

[71] K.S. Chou, Y.C. Chang, L.H. Chiu, Studies on the Continuous Precipitation of Silver Nanoparticles, *Industrial & Engineering Chemistry Research* 51 (2012) 4905-4910.

[72] A. Knauer, A. Csaki, W. Fritzsche, C.A. Serra, N. Leclerc, J.M. Kohler, Micro continuous flow-through synthesis of triangular silver nanoprisms and their incorporation in complexly composed polymer microparticles, *Chemical Engineering Journal* 227 (2013) 191-197.

[73] D.V.R. Kumar, B.L.V. Prasad, A.A. Kulkarni, Segmented flow synthesis of Ag nanoparticles in spiral microreactor: Role of continuous and dispersed phase, *Chemical Engineering Journal* 192 (2012) 357-368.

[74] C.S. Senej, B.M. Gutzman, R.H. Goddard, Correlation of Size and Surface-Enhanced Raman Scattering Activity of Optical and Spectroscopic Properties for Silver Nanoparticles, *Journal of Physical Chemistry C* 113 (2009) 74-80.

[75] S. Agnihotri, S. Mukherji, S. Mukherji, Size-controlled silver nanoparticles synthesized over the range 5–100 nm using the same protocol and their antibacterial efficacy, *RSC Advances* 4 (2014) 3974-3983.

[76] N.T.K. Thanh, N. Maclean, S. Mahiddine, Mechanisms of Nucleation and Growth of Nanoparticles in Solution, *Chemical Reviews* 114 (2014) 7610-7630.

[77] M.Q. Lu, S.K. Yang, Y.P. Ho, C.L. Grigsby, K.W. Leong, T.J. Huang, Shape-Controlled Synthesis of Hybrid Nanomaterials via Three-Dimensional Hydrodynamic Focusing, *Acs Nano* 8 (2014) 10026-10034.

[78] A. Jahn, S.M. Stavis, J.S. Hong, W.N. Vreeland, D.L. Devoe, M. Gaitan, Microfluidic Mixing and the Formation of Nanoscale Lipid Vesicles, *Acs Nano* 4 (2010) 2077-2087.